Exact Amplitude–Delay Information Crossover for an Idealized Helical DAS Array

Yuanyuan Cao, Ning Hu, Chengtao Huang, and Kunjie Shi

***Abstract*—Helical distributed acoustic sensing (DAS) geometries couple directional strain amplitude and propagation phase, yet their respective contributions to bearing information and their compatibility with practical extraction chains are usually left implicit. For an idealized point-channel helix with unknown complex source amplitude, we prove an exact finite-array frequency at which amplitude and delay information are equal and derive a continuous full-turn corollary exposing radius, pitch, winding-angle, and elevation dependence. The finite expression matches a separately constructed information ratio on 723 prespecified geometries to a maximum relative error of 4.24×10^{-15}. Because an array-domain bound is comparable to a processing-chain estimate only under compatible observation constructions, we also audit a prespecified Hann–DFT–MUSIC chain. Its long, bin-aligned records match the array-domain pseudo-true bearing, whereas short zero-padded controls do not. A 118,500-estimate study then validates local sandwich variance and its combination with squared pseudo-true bias over prespecified mismatch conditions. These are model-level information and compatibility results, not field-performance bounds for gauge-averaged cables.**

***Index Terms*—Distributed acoustic sensing, direction of arrival, Fisher information, helical array, model misspecification, pseudo-true parameter.**

I. Introduction

HELICALLY wound fibers trade axial sensitivity for broader directional response, but the response depends on winding geometry, material properties, and mechanical coupling [1], [2]. Field trials confirm broadside sensitivity while also showing that ideal wrapping-angle predictions need not transfer unchanged to deployed cables [3], [4]. At the signal-processing level, DAS channels differ from omnidirectional point sensors because strain projection, gauge-length averaging, pulse shape, and cable transfer all modify the observed array response [5], [6], [7], [8].

Two questions follow. First, when the same geometry controls element amplitude and propagation phase, which mechanism supplies bearing information at a given frequency? Second, when an ideal array bound is compared with a segmented real-signal pipeline, do both objects describe the same observation construct? Hu *et al.* developed branch-aware phase-to-bearing diagnostics and archived the Hann–DFT–MUSIC outputs used as comparators here [9]; that study did not address the amplitude–delay information crossover. Directional-sensor CRBs [10], classical MUSIC/ML/CRB analysis [11], and misspecified-likelihood theory [12], [13], [14] provide the required tools.

We derive an exact, grid-free crossover for a finite sampled helix and a helix-specific full-turn law with measured finite-aperture error. The real-envelope/pure-phase orthogonality behind the decomposition is not limited to helices; the projected finite-helix quadratic forms and their geometry reduction are the specific results. Mechanism ablations and resource-defined baselines place the information result in context. Paired outputs from the previously reported processing chain, record-construction controls, and a local misspecified-ML sandwich study then test when the same manifold has a compatible processing-chain interpretation.

This work was supported by the State Key Laboratory of Ocean Engineering, Shanghai Jiao Tong University (Grant No. GKZD010089), and the State Key Laboratory of Acoustics and Marine Information, Chinese Academy of Sciences (Grant No. SKLA202406). (Corresponding author: Ning Hu.)

Yuanyuan Cao is with the School of Communication Engineering, Hangzhou Dianzi University, Hangzhou 310018, China. Ning Hu, Chengtao Huang, and Kunjie Shi are with the School of Mechanical Engineering, Hangzhou Dianzi University, Hangzhou 310018, China (e-mail: yuany.c@hdu.edu.cn; jluhooning@163.com; chengtaohuang@hdu.edu.cn; kunjie_shi@hdu.edu.cn).

II. Finite-Array Information Crossover

A. Point-channel manifold

For channel i, let $\mathbf{r}_i$ and $\mathbf{t}_i$ denote position and unit tangent. A longitudinal plane wave has point strain proportional to $\mathbf{u}\mathbf{u}^{\mathsf{T}}$, so tangential axial strain is proportional to $(\mathbf{t}_i^{\mathsf{T}}\mathbf{u})^2$; the snapshot amplitude below absorbs the common strain scalar [1]. With $\mathbf{u}(\theta, \phi) = [\cos\phi\cos\theta, \cos\phi\sin\theta, \sin\phi]^{\mathsf{T}}$, the specified manifold is

$$a_i = q_i^2 e^{-\mathrm{j}k\mathbf{r}_i^{\mathsf{T}}\mathbf{u}}, \quad q_i = \mathbf{t}_i^{\mathsf{T}}\mathbf{u}, \quad k = 2\pi f/c. \tag{1}$$

We treat elevation ϕ as known and estimate azimuth θ; a joint azimuth–elevation bound would require an additional Schur complement. Coherent snapshots obey $\mathbf{y}_\ell = \beta_\ell \mathbf{a} + \mathbf{n}_\ell$, where β_ℓ is an unknown complex amplitude and $\mathbf{n}_\ell \sim \mathcal{CN}(\mathbf{0}, \sigma^2\mathbf{I})$. Define the dimensionless accumulated energy SNR as $\rho_E = \sum_\ell |\beta_\ell|^2/\sigma^2$. Eliminating β_ℓ gives

$$F_{\theta\theta} = 2\rho_E \operatorname{Re}\{\mathbf{a}_\theta^{\mathsf{H}}\mathbf{P}_{\mathbf{a}}^{\perp}\mathbf{a}_\theta\}, \quad \mathbf{P}_{\mathbf{a}}^{\perp} = \mathbf{I} - \frac{\mathbf{a}\mathbf{a}^{\mathsf{H}}}{\mathbf{a}^{\mathsf{H}}\mathbf{a}}. \tag{2}$$

This is an idealized point-channel model. It excludes gauge integration, cable–medium coupling, and channel-dependent transfer functions. All angular derivatives and information quantities use radians; degrees appear only in reported errors and standard deviations.

B. Exact decomposition and crossover

Define $q_{\theta,i} = \mathbf{t}_i^{\mathsf{T}}\mathbf{u}_\theta$, $h_i = \mathbf{r}_i^{\mathsf{T}}\mathbf{u}_\theta$, and

$$\mathbf{g} = q^2, \qquad \mathbf{x} = 2q \odot q_\theta, \qquad \mathbf{z} = q^2 \odot h, \qquad \mathbf{P}_{\mathbf{g}}^{\perp} = \mathbf{I} - \frac{\mathbf{g}\mathbf{g}^{\mathsf{T}}}{\mathbf{g}^{\mathsf{T}}\mathbf{g}}.$$

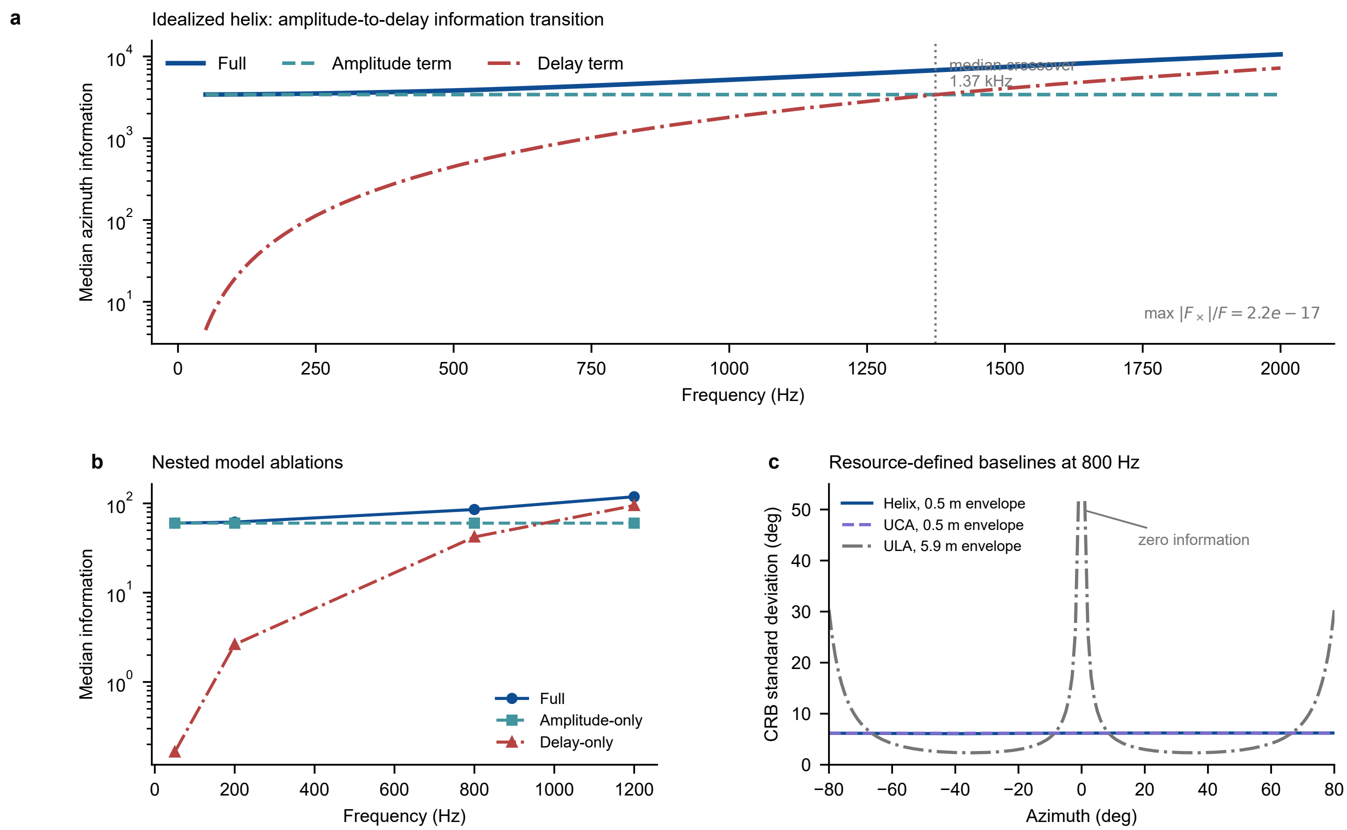

Fig. 1. Information structure and resource-defined baselines. (a) Median projected azimuth information: the amplitude term is frequency invariant, the delay term scales as f^2, and their mixed term is numerically zero. Panel (a) uses $\rho_E = 100$. (b) Amplitude-only and delay-only nested manifolds are mechanism ablations, not additive shares of the full model. (c) At 800 Hz, the helix and same-0.5 m-transverse-envelope UCA have similar median bounds; the same-fiber-length ULA uses an 11.8-times larger envelope and has zero information at broadside. Panels (b)–(c) use $\rho_E = 1$; absolute scales are not compared across panels.

Assume $\mathbf{g}^\mathsf{T}\mathbf{g} > 0$.

Theorem 1 (Finite-array helical crossover): For the manifold in (1), after eliminating the unknown per-snapshot complex amplitudes,

$$F_{\theta\theta} = F_A + F_\tau, \tag{3}$$

$$F_A = 2\rho_E \mathbf{x}^\mathsf{T}\mathbf{P}_\mathbf{g}^\perp \mathbf{x}, \quad F_\tau = 2\rho_E k^2 \mathbf{z}^\mathsf{T}\mathbf{P}_\mathbf{g}^\perp \mathbf{z}. \tag{4}$$

The mixed term is identically zero. If both quadratic forms are positive, the unique positive equality frequency is

$$\boxed{f_\times = \frac{c}{2\pi}\sqrt{\frac{\mathbf{x}^\mathsf{T}\mathbf{P}_\mathbf{g}^\perp \mathbf{x}}{\mathbf{z}^\mathsf{T}\mathbf{P}_\mathbf{g}^\perp \mathbf{z}}}.} \tag{5}$$

Proof sketch: $\mathbf{a}_\theta = \mathbf{D}(\mathbf{x} - \mathrm{j}k\mathbf{z})$, where $\mathbf{D} = \mathrm{diag}\{\exp(-\mathrm{j}k\mathbf{r}_i^\mathsf{T}\mathbf{u})\}$. Removing this unitary diagonal phase factor reduces the nuisance projection to $\mathbf{P}_\mathbf{g}^\perp$. The projected amplitude derivative is real and the projected delay derivative is purely imaginary, so their real inner product vanishes. Equation (5) follows because F_A is constant in f and F_τ is proportional to f^2. The full algebra and degeneracy cases are given in the Supplementary Material.

The orthogonality mechanism applies more generally to real-envelope phased manifolds under the same white-noise metric. The helix-specific quantities are the projected forms in (5) and their geometry reduction below. The result is independent of ρ_E and requires no frequency-grid search. If only the numerator in (5) vanishes, $f_\times = 0$; if only the denominator vanishes, no finite crossover exists; if both vanish, azimuth is locally unidentifiable. Denote the real mixed contribution by $F_{A\tau}$. On the 28,920-point information scan, $\max|F_{A\tau}|/F_{\theta\theta} = 2.2 \times 10^{-17}$. Figure 1(a) shows the predicted constant and f^2 laws.

The nested manifolds in Fig. 1(b) isolate mechanisms but are not additive contributions because nuisance projection changes with the manifold. At 800 Hz, the helix and same-0.5 m-transverse-envelope UCA have median CRB standard deviations of 6.200° and 6.167°, respectively. The same-5.9 m-fiber-span ULA reaches a lower median bound but uses an 11.8-times larger physical envelope and loses all broadside information [Fig. 1(c)]. Thus, the evidence supports stable angular coverage, not unconditional helical superiority.

III. Continuous Full-Turn Geometry Law

Let the winding angle α be measured from the transverse plane, so that $p = 2\pi R \tan\alpha$. For continuous, uniform arc-length averaging over complete turns, define $A = \cos\alpha\cos\phi$ and $B = \sin\alpha\sin\phi$.

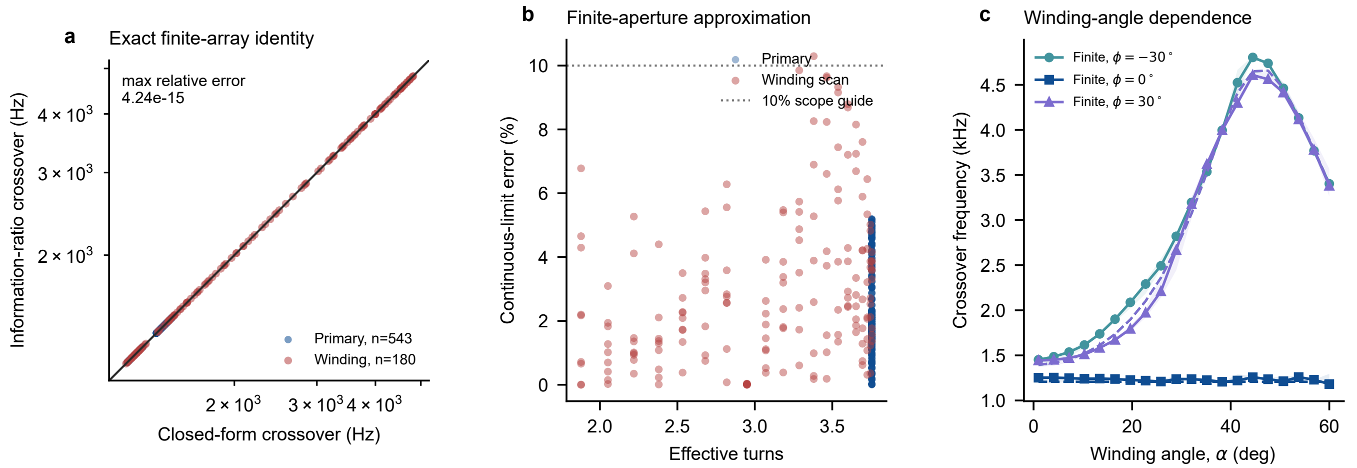

Fig. 2. Closed-form crossover verification. (a) The finite-array expression matches a separately constructed information ratio on all 723 prespecified geometries. (b) Relative error of the continuous full-turn corollary versus effective turn count. (c) Winding-angle dependence; solid curves are finite-array medians, shading spans the sampled azimuths, and dashed curves are the continuous limit.

Corollary 1 (Continuous full-turn crossover): For $R > 0$, $|\phi| < \pi/2$, and $Q_A, Q_{D0} > 0$, period averaging of Theorem 1 gives

$$Q_A = \frac{A^2(A^2 + 4B^2)}{2}, \tag{6}$$

$$Q_{D0} = \frac{15A^8 - 60A^6B^2 + 160A^4B^4 - 32A^2B^6 + 64B^8}{16(3A^4 + 24A^2B^2 + 8B^4)}, \tag{7}$$

$$f_{\times,\infty} = \frac{c}{2\pi R\cos\phi}\sqrt{\frac{Q_A}{Q_{D0}}}. \tag{8}$$

At $|\phi| = \pi/2$, azimuth is locally unidentifiable. Vanishing Q_A or Q_{D0} follows the finite-array degeneracy classification rather than (8). At $\phi = 0$ and away from degeneracy,

$$f_{\times,\infty} = \frac{c}{2\pi R}\sqrt{\frac{8}{5}},$$

which is independent of α. Moreover, $\partial \ln f_\times / \partial \ln R = -1$. At fixed R, $\partial \ln f_\times / \partial \ln p = \sin\alpha\cos\alpha\, \partial \ln f_\times / \partial\alpha$. We use the finite expression for quantitative predictions; the continuous corollary separates radius scaling from pitch–angle coupling.

Across 543 primary tracks, (5) gives one crossover in $1.182\,\mathrm{kHz}$ to $1.472\,\mathrm{kHz}$, with median $1.369\,\mathrm{kHz}$. Its maximum relative discrepancy from the separately constructed information ratio is 4.24×10^{-15} [Fig. 2(a)]. Linear interpolation on the original grid incurs 0.134% median and 0.164% maximum error. The continuous corollary has 1.91% median and 5.19% maximum error on these tracks. On the wider 180-track winding scan, the corresponding errors are 2.39% and 10.29% over the prespecified range of 1.878–3.755 effective turns [Fig. 2(b)–(c)]. These empirical discrepancies are not error bounds for arbitrary finite apertures.

IV. Compatibility with a Segmented Hann–DFT–MUSIC Chain

Let $\mathbf{a}_t$ be the perturbed true array vector and $\mathbf{a}_m(\theta)$ the nominal vector. Under the shared-amplitude model, the pseudo-true bearing is

$$\theta_{\mathrm{pt}} = \arg\max_{\theta} \frac{|\mathbf{a}_m^{\mathsf{H}}(\theta)\mathbf{a}_t|^2}{\|\mathbf{a}_m(\theta)\|_2^2\|\mathbf{a}_t\|_2^2}. \tag{9}$$

For the sandwich experiment, K iid snapshots share a fixed complex amplitude γ and use $\boldsymbol{\eta} = (\theta, \operatorname{Re}\gamma, \operatorname{Im}\gamma)$. With per-snapshot score $\mathbf{s}_1 = \partial\ell_1/\partial\boldsymbol{\eta}$, $\mathbf{A}_1 = -\mathbb{E}_t[\partial^2\ell_1/\partial\boldsymbol{\eta}\partial\boldsymbol{\eta}^{\mathsf{T}}]$, and $\mathbf{B}_1 = \mathbb{E}_t[\mathbf{s}_1\mathbf{s}_1^{\mathsf{T}}]$ at θ_{pt}, the local misspecified-ML variance is

$$C_{\mathrm{sand},K} = \frac{1}{K}\left[\mathbf{A}_1^{-1}\mathbf{B}_1\mathbf{A}_1^{-1}\right]_{\theta\theta}. \tag{10}$$

The nominal crossover FIM permits arbitrary deterministic β_ℓ through ρ_E; the asymptotic experiment in (10) instead fixes γ across iid snapshots. Relative to the physical direction $\theta^\star$,

$$\mathrm{MSE}_{\theta^\star} \approx C_{\mathrm{sand},K} + (\theta_{\mathrm{pt}} - \theta^\star)^2. \tag{11}$$

Here $C_{\mathrm{sand},K}$ has units of radians squared [12], [13], [14]. Equation (9) is an array-domain likelihood quantity; it is not automatically the bearing returned by the segmented Hann–DFT–MUSIC chain reported in [9]. We therefore define a pipeline gap as the paired difference between those two outputs for the same geometry realization and direction.

A. Paired output agreement

Fifty prespecified geometry realizations at $0°, 30°, 60°$ give 150 pairings between the continuous pseudo-true optimum and the archived single-record noiseless Hann–DFT–MUSIC output of [9]. Their median absolute pipeline gap is 2.23×10^{-5} degrees [Fig. 3(a)]. Two independent continuous optimizers agree within 5.39×10^{-12} degrees; complete objective profiles show no near-parallel competing branch. This paired audit uses the same prespecified geometry metadata and direction in both chains; it tests compatibility, not independent physical validation.

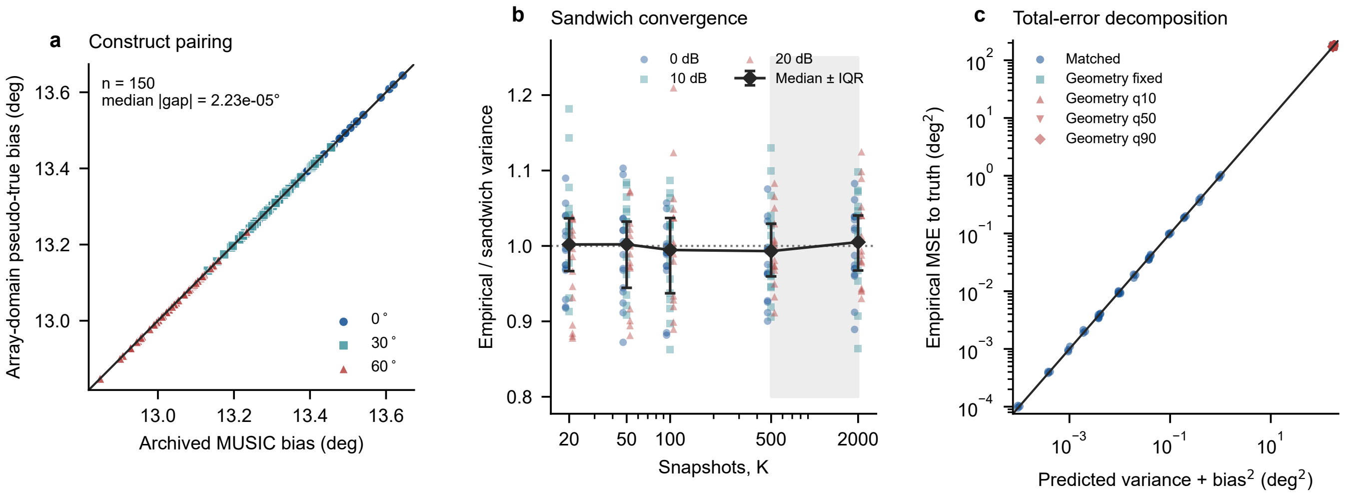

Fig. 3. Pipeline-compatibility and misspecification validation. (a) Array-domain pseudo-true bias versus the prespecified pipeline bias. (b) Empirical-to-sandwich variance ratio versus snapshot count. (c) Empirical total error versus local sandwich variance plus squared pseudo-true bias.

B. Record-construction audit

A separate bridge audit uses five scenarios at the same three bearings. All 15 long, bin-aligned cases pass, whereas all 15 short zero-padded negative controls fail. The negative control shows that compatibility depends on record construction; it neither diagnoses a universal estimator failure nor transfers the sandwich variance to arbitrary end-to-end MUSIC outputs.

C. Local covariance and total error

The sandwich study covers 15 prespecified scenarios, SNRs of $\{0, 10, 20\}$ dB, and $K = \{20, 50, 100, 500, 2000\}$: 225 conditions and 118,500 Monte Carlo estimates. The empirical-to-predicted variance ratio has median 0.9979 and range 0.8625–1.2097; every prespecified high-snapshot condition passes and no branch jump is observed [Fig. 3(b)]. Empirical total error also tracks the sum in (11) over more than six orders of magnitude [Fig. 3(c)]. This establishes local convergence around $\theta_{\rm pt}$ separately from the deterministic offset to $\theta^\star$.

V. Validation Scope and Limitations

For the 60-channel nominal helix ($R = 0.25\,\mathrm{m}$, $p = 0.02\,\mathrm{m}$, $0.1\,\mathrm{m}$ fiber-arc spacing), the finite identity holds on 723/723 tracks, the continuous-law primary median/maximum discrepancy is 1.91%/5.19%, and $\max |F_{A\tau}|/F_{\theta\theta} = 2.2 \times 10^{-17}$ over 28,920 points. Independent regeneration on local and cloud platforms gave maximum absolute differences of 2.25×10^{-13}, 4.13×10^{-11}, and zero for the construct, baseline, and scope audits. The public archive and accompanying Information for Reproducibility provide figure source tables, hashes, tests, and one-command execution. The archived package is available at https://doi.org/10.5281/zenodo.21603787.

The closed form is identity-based rather than fitted, whereas the sandwich result concerns estimator convergence, not the physical cable model; neither can compensate for an incompatible observation construction.

At $800\,\mathrm{Hz}$, the same-envelope UCA and helix differ by only 0.53% in median CRB standard deviation. The long ULA can perform better over favorable directions, but uses an 11.8-times larger envelope and has a broadside null. Thus, the helix offers compact, nonzero coverage in the scanned sector, not universal array optimality.

The conclusions remain model-bounded. Gauge length changes usable spatial content [6], [7], [8], coupling and material properties alter the response [1], and the simulated geometry perturbations do not represent a manufacturing population. The model also excludes random channel gain, phase drift, colored noise, and IQ nonidealities.

VI. Conclusion

Within these boundaries, the coupled helical manifold has an exact finite-array amplitude–delay crossover and a continuous law with measured finite-aperture error. Its processing-chain interpretation requires local convergence and observation-model compatibility, established here only for the prespecified long, bin-aligned point-channel construction.

Acknowledgment

During the preparation of this work, the authors used OpenAI Codex to support language editing, organization of manuscript drafts, and consistency checks throughout the manuscript and supplementary files. The authors reviewed, edited, and verified all AI-assisted output, including numerical claims and references, and take full responsibility for the content of the publication.

References

[1] B. N. Kuvshinov, "Interaction of helically wound fibre-optic cables with plane seismic waves," *Geophysical Prospecting*, vol. 64, no. 3, pp. 671–688, 2016.

[2] A. F. Baird, "Modelling the response of helically wound DAS cables to microseismic arrivals," in *First EAGE Workshop on Fibre Optic Sensing*. European Association of Geoscientists & Engineers, 2020, pp. 1–5.

[3] J. C. Hornman, "Field trial of seismic recording using distributed acoustic sensing with broadside sensitive fibre-optic cables," *Geophysical Prospecting*, vol. 65, no. 1, pp. 35–46, 2017.

[4] S. Masaya, R. Naruse, and Y. Kobayashi, "Comparative earthquake sensitivity of straight and triply helical fibers in surface distributed acoustic sensing," *Scientific Reports*, 2026, early access.

[5] S. P. Näsholm, K. Iranpour, A. Wuestefeld, B. D. E. Dando, A. F. Baird, and V. Oye, "Array signal processing on distributed acoustic sensing data: Directivity effects in slowness space," *Journal of Geophysical Research: Solid Earth*, vol. 127, no. 2, p. e2021JB023587, 2022.

[6] P. G. Hubbard, J. P. Vantassel, B. R. Cox, J. W. Rector, M. B. S. Yust, and K. Soga, "Quantifying the surface strain field induced by active sources with distributed acoustic sensing: Theory and practice," *Sensors*, vol. 22, no. 12, p. 4589, 2022.

[7] A. Sayed, R. Bachrach, A. Titova, and G. Busanello, "Research note: Choosing gauge length for surface distributed acoustic sensing," *Geophysical Prospecting*, vol. 72, no. 8, pp. 2893–2901, 2024.

[8] T. Cuny, P. Bettinelli, and J. Le Calvez, "Variable gauge length: Processing theory and applications to distributed acoustic sensing," *Geophysical Prospecting*, vol. 73, no. 1, pp. 160–187, 2025.

[9] N. Hu, Y. Cao, C. Huang, and K. Shi, "Branch-aware phase-to-bearing diagnostics in an idealized helical DAS phase array," Engineering Archive, preprint, Jul. 2026, posted July 27, 2026, doi: 10.31224/7727.

[10] M. Dibiase, M. Mohammadgholiha, and L. De Marchi, "Optimal array design and directive sensors for guided waves DoA estimation," *Sensors*, vol. 22, no. 3, p. 780, 2022.

[11] P. Stoica and A. Nehorai, "MUSIC, maximum likelihood, and Cramer–Rao bound," *IEEE Transactions on Acoustics, Speech, and Signal Processing*, vol. 37, no. 5, pp. 720–741, 1989.

[12] H. White, "Maximum likelihood estimation of misspecified models," *Econometrica*, vol. 50, no. 1, pp. 1–25, 1982.

[13] C. D. Richmond and L. L. Horowitz, "Parameter bounds on estimation accuracy under model misspecification," *IEEE Transactions on Signal Processing*, vol. 63, no. 9, pp. 2263–2278, 2015.

[14] S. Fortunati, F. Gini, M. S. Greco, and C. D. Richmond, "Performance bounds for parameter estimation under misspecified models: Fundamental findings and applications," *IEEE Signal Processing Magazine*, vol. 34, no. 6, pp. 142–157, 2017.